

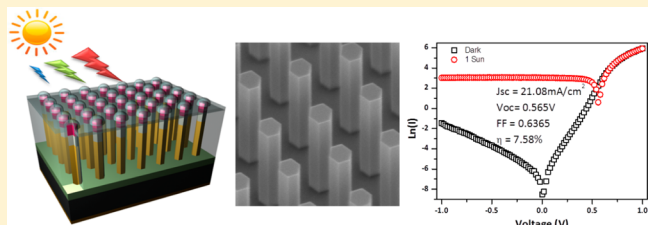
GaAs Nanowire Array Solar Cells with Axial p–i–n Junctions

Maoqing Yao, Ningfeng Huang, Sen Cong, Chun-Yung Chi, M. Ashkan Seyed, Yen-Ting Lin, Yu Cao, Michelle L. Povinelli, P. Daniel Dapkus,* and Chongwu Zhou*

Ming Hsieh Department of Electrical Engineering and Center for Energy Nanoscience, University of Southern California, Los Angeles, California 90089, United States

Supporting Information

ABSTRACT: Because of unique structural, optical, and electrical properties, solar cells based on semiconductor nanowires are a rapidly evolving scientific enterprise. Various approaches employing III–V nanowires have emerged, among which GaAs, especially, is under intense research and development. Most reported GaAs nanowire solar cells form p–n junctions in the radial direction; however, nanowires using axial junction may enable the attainment of high open circuit voltage (V_{oc}) and integration into multijunction solar cells. Here, we report GaAs nanowire solar cells with axial p–i–n junctions that achieve 7.58% efficiency. Simulations show that axial junctions are more tolerant to doping variation than radial junctions and lead to higher V_{oc} under certain conditions. We further study the effect of wire diameter and junction depth using electrical characterization and cathodoluminescence. The results show that large diameter and shallow junctions are essential for a high extraction efficiency. Our approach opens up great opportunity for future low-cost, high-efficiency photovoltaics.



KEYWORDS: Nanowires, solar cells, gallium arsenide, axial junction, MOCVD

In recent years, solar cells based on semiconductor nanowires have been a topic of intense research and development for next-generation photovoltaics.^{1–21} One approach to surpass the Shockley–Queisser efficiency limit is to use multijunction solar cells containing several p–n junctions in series.^{22–26} Each junction is designed to absorb a specific wavelength range of sun light, reducing thermalization losses, and thereby increasing efficiency (Supporting Information, Figure S1a). Traditional, monolithically integrated multijunction solar cells consist of sequentially stacked thin films. The lattice constants of the materials used are matched to allow high-quality epitaxial growth. GaAs and germanium are currently the most widely used substrates since there are lattice matched materials with larger bandgaps suitable for forming a current matched set of junctions. These substrates contribute a large portion of the total material cost and prevent large-scale terrestrial implementation. The small footprint of nanowires allows them to accommodate lattice-mismatch induced strain through elastic relaxation at the edges.^{27–32} This capability offers great freedom in choosing growth substrates, which are otherwise infeasible in the planar thin film scenario. For instance, dislocation-free InP or GaAs nanowires can be grown on a silicon substrates,^{32–35} significantly reducing substrate cost and enabling use of the existing silicon industry infrastructure (Supporting Information, Figure S1b). Meanwhile, the freedom to use multiple, stacked, nonlattice-matched materials within each nanowire allows the construction of multijunction cells with optimal band gap combinations (Supporting Information, Figure S1c). In addition, both simulation and experiments have shown that nanowires are inherently excellent light absorbers due to light

scattering and the effect of resonant modes, even without additional antireflection coatings.^{11,36–43}

Among various nanowires, those made from III–V compound semiconductor materials are considered as some of the most promising platforms for photovoltaics due to high absorption, direct band gap, superior carrier mobility, and well-developed synthesis techniques. Significant progress with InP nanowire solar cells has recently been reported especially with axial p–i–n junctions.^{18,21,44} In contrast, GaAs is another important material with suitable bandgap and has the advantage that gallium is more abundant than indium. However, progress in the development of GaAs nanowire solar cells has been relatively slow, and their potential has not been fully exploited. Previous work on GaAs nanowire solar cells focused on radial p–n or p–i–n junctions. For example, in 2008, LaPierre et al.⁵ reported pioneering work of a GaAs nanowire array based solar cell with core/shell radial junction and power conversion efficiency (PCE) of 0.83%. In 2009, Fontcuberta i Morral et al.⁴⁵ reported a single GaAs nanowire solar cell with PCE of 4.5% by molecular beam epitaxy, and their V_{oc} close to 1 V indicates high-quality radial p–i–n junctions. In 2011, Mariani et al.⁷ demonstrated solar cells made from lithographically patterned GaAs nanorod arrays with radial junctions and exhibited a PCE of 2.54%, which represented excellent progress toward large area realization. Recently Tegude et al.²⁰ reported

Received: February 24, 2014

Revised: May 16, 2014

Published: May 21, 2014



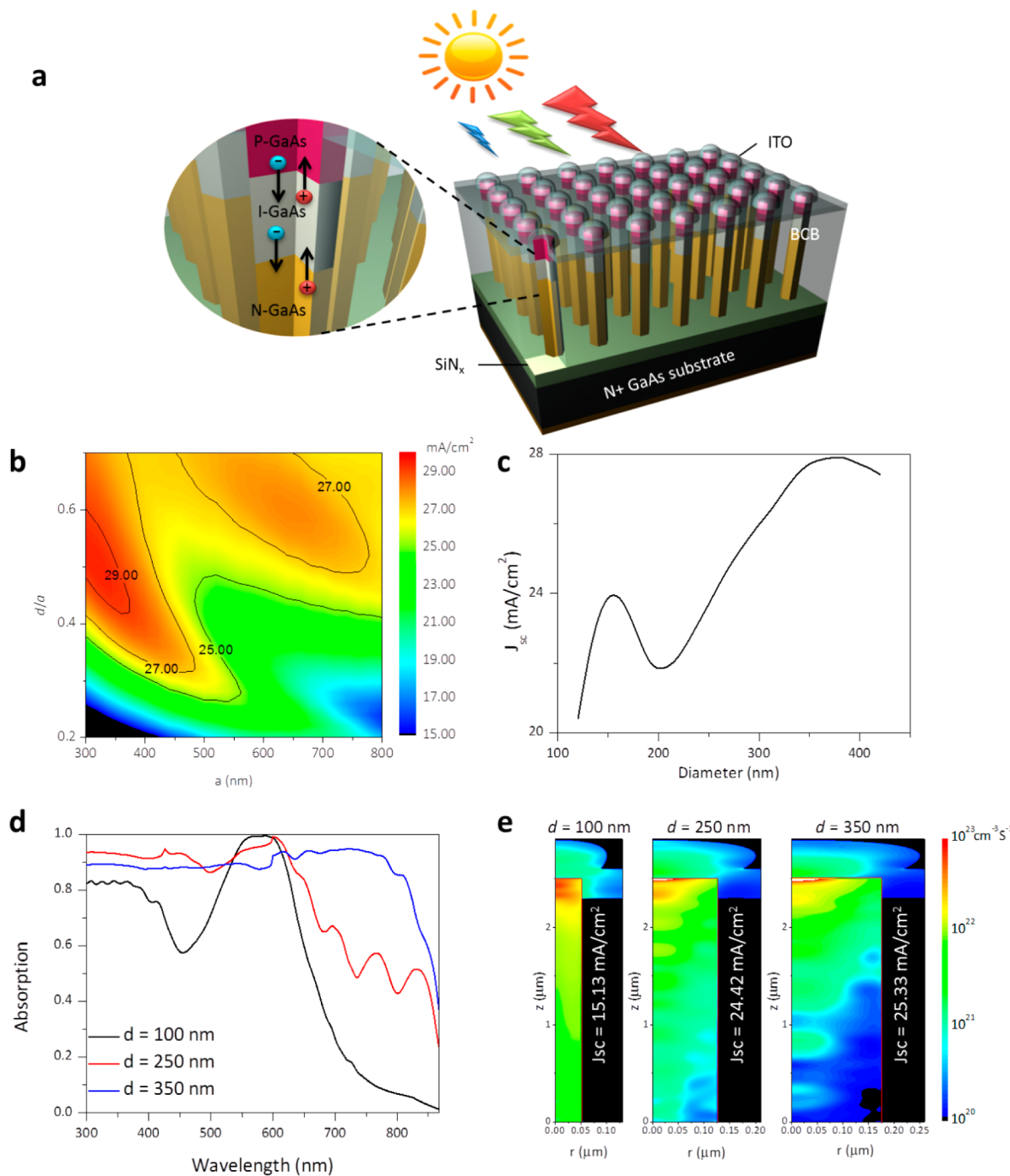


Figure 1. Device structure and optical absorption simulation. (a) Schematic of a solar cell made from GaAs nanowires with axial junctions. Carrier flow direction in solar cell operation under sunlight is shown in the zoomed-in graph of the junction. (b) Maximum achievable J_{sc} (mA/cm^2) versus pitch a and diameter/pitch ratio d/a . Nanowires are 3 μm tall and grown on a GaAs substrate. (c) Maximum achievable J_{sc} versus nanowire diameter for a fixed pitch of 600 nm and height of 3 μm . (d) Absorption spectra of nanowire arrays with 600 nm pitch and 100 nm (black), 250 nm (red), and 350 nm (blue) diameter. (e) Carrier generation rate profile under AM 1.5G solar spectrum for nanowires embedded in BCB and capped by ITO for diameters of 100, 250, and 350 nm.

a single GaAs/InGaP/GaAs with a radial p-i-n junction with a PCE of 4.7%. Recent efforts on in situ passivation of GaAs nanowires with lattice-matched wide band gap materials revealed encouraging improvements in the short circuit current. By growing a lattice-matched InGaP passivation layer, a quantum efficiency close to unity has been observed leading to reported PCE between 4% and 7.43%.^{15,19}

In contrast, solar cells based on axial p-n or p-i-n junctions have not been fully studied, although it is intriguing to compare their performance to that of radial junction devices and study the underlying science. Our recent theoretical study (Huang et al.³⁷) indicates that axial junctions are more sensitive to the presence of surface states, but axial junctions provide higher V_{oc} and more flexibility in the design of junction structure such as the thickness of base and emitter layers than radial junctions.

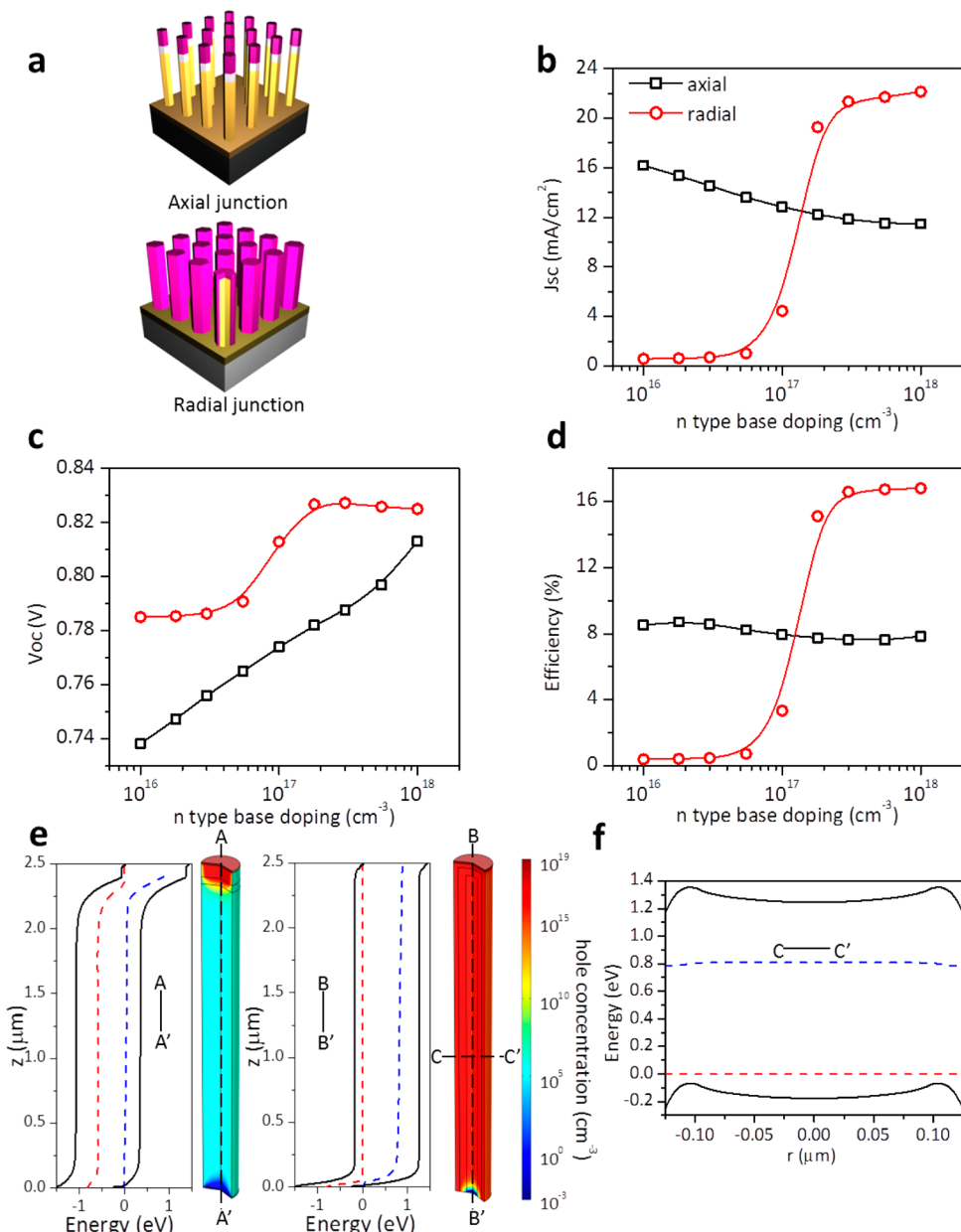


Figure 2. Comparison between nanowire solar cells with axial junctions and radial junctions. (a) Schematic diagram of axial (upper) and radial (lower) junctions in nanowires. (b) J_{sc} (c) V_{oc} , and (d) efficiency of nanowire solar cells with axial junctions (black) and radial junctions (red) versus doping concentration in the n-type base. The surface recombination velocity is $3 \times 10^5 \text{ cm/s}$. See text for details of junction geometry and doping concentration. (e) 3D mapping of hole concentration in the dark and in thermal equilibrium for the axial junction (left) and the radial junction (right). Band diagrams under AM 1.5 short circuit conditions along the center of each nanowire (A–A' and B–B') are shown on the left together with quasi Fermi levels of electrons (blue dashed line) and holes (red dashed line). (f) Band diagram along C–C' line in the radial junction in (e) together with quasi Fermi levels of electrons and holes.

Furthermore, a single axial junction is of considerable technical importance, as it is an important building block for multi-junction solar cells with three or more junctions as shown in Figure S1c. Nanowires with junctions stacked in the axial direction provide an intuitive analogue to the traditional thin film multijunction solar cells where the incident light can pass from materials with larger bandgap to those with lower bandgap sequentially.

Here, we report solar cells based on GaAs nanowires with axial p–i–n junctions that achieve a PCE of 7.58%. This value is so far the highest reported PCE for any solar cells made from GaAs nanowire arrays. We carry out optical simulations to

systematically study the light absorption properties of GaAs nanowire arrays. A theoretical comparison between radial and axial junction solar cells is conducted, which reveals that the axial junction design is more tolerant to doping variation. For a particular doping range, axial junction designs can offer better performance. Under the guidance of these simulations, we experimentally demonstrate solar cells based on uniformly patterned GaAs nanowire arrays with axial p–i–n junctions via selective area growth (SAG) in metal–organic chemical vapor deposition (MOCVD). Two key design parameters are studied to optimize device characteristics. Our results indicate that nanowires with shallower junctions offer better performance

than deeper junctions, and large wire diameters can lead to a short circuit current density (J_{sc}) as high as 23.28 mA/cm^2 in the absence of any surface passivation treatment. The junction depth dependence is further investigated and explained by cathodoluminescence measurements.

Figure 1a is a schematic of a solar cell made from a vertically aligned GaAs nanowire array grown on a GaAs substrate. Nanowires are embedded in transparent insulating polymer BCB, for mechanical support and covered by a transparent conductive indium tin oxide (ITO) front contact to let sunlight pass through. Incident light generates electrons and holes which flow toward the n-type and p-type region, respectively. The absorption properties of periodic nanowire arrays strongly depend on the array structure. To determine the optimal structure for absorption, we first carry out full-vectorial electromagnetic simulations (see Supporting Information for details) to calculate the absorption of nanowire arrays with different diameters and pitch. We calculate the maximum achievable short circuit current from the optical absorption by assuming unity external quantum efficiency. Figure 1b shows J_{sc} as a function of pitch, a , and diameter-to-pitch ratio, d/a , for a nanowire height of $3 \mu\text{m}$. Calculations were performed using the AM 1.5G solar spectrum assuming an infinitely thick GaAs substrate. Two local maxima are observed on this map. One is at $a = 300 \text{ nm}$ and $d/a = 0.55$, and the other one is around $a = 650 \text{ nm}$ and $d/a = 0.6$. We focus on the maximum point associated with pitch of 650 nm due to the fact that, without sacrificing too much absorption ($<1 \text{ mA/cm}^2$), a larger pitch eases fabrication requirements. Furthermore, we will show later in the paper that the small diameter of the other maximum point is unfavorable for the electrical properties. In Figure 1c, we plot J_{sc} versus nanowire diameter for a fixed pitch of 600 nm and height of $3 \mu\text{m}$. We can achieve J_{sc} as high as 28 mA/cm^2 for a nanowire array with a diameter of 350 nm , which is close to the theoretical limit of a single junction GaAs solar cell. Comparing the absorption spectra of arrays with diameters of 100 , 250 , and 350 nm (600 nm pitch, $3 \mu\text{m}$ height) shown in Figure 1d, the 350 nm one enhances the absorption by filling in the low absorption dips between 400 and 550 nm and between 700 and 900 nm that appear in the spectra of the 100 and 250 nm diameter wire arrays. We also plot the spatial carrier generation rate distribution within the realistic nanowire array structure (with the BCB polymer and ITO caps) for nanowires with height of $2.5 \mu\text{m}$ and diameters of 100 , 250 , and 350 nm , respectively (Figure 1e). The maximum achievable short circuit currents are also indicated in each profile. More discussion about the local minimum around 200 nm in Figure 1c can be found in the Supporting Information.

In terms of electrical properties, the design of the p–n junction governs the overall performance of a solar cell. We thus carefully examined the operational conditions of nanowire solar cells with radial and axial junctions. Figure 2a shows schematics of these two junctions in the nanowires. We numerically solve the current density–voltage (J – V) response (see Supporting Information for details) of the nanowire solar cells with a 600 nm pitch, 250 nm diameter, and $2.5 \mu\text{m}$ height. We use Synopsys Sentaurus to solve the drift-diffusion equations for carrier transport within the nanowires. The nanowires are subject to AM 1.5G solar irradiation. The position-dependent carrier generation rate is determined from the optical absorption simulations above and is shown in Figure 1e. For the axial junction, the p-type segment is on top, with a thickness of 100 nm , and for the radial junction, the p-type

region is on the outside, with a thickness of 30 nm . Both intrinsic regions are 50 nm thick. The thicknesses of the p-type regions were chosen based on our previous study.³⁷ The thicker shell lead to degraded performance as shown in simulations presented in Figure S4. We assume that the doping-dependent mobilities for electrons and holes are the same as in the bulk, with a Shockley–Read–Hall (SRH) recombination lifetime of 1 ns . Both donor-like and acceptor-like surface state densities are fixed to be $1.5 \times 10^{12} \text{ cm}^{-2}$, corresponding to a surface recombination velocity (SRV) of $30,000 \text{ cm/s}$. We fix the doping concentration of the p-type emitters to be 10^{18} cm^{-3} for the purpose of forming a low resistance ohmic contact, and vary the n-type base doping in both the axial and radial junctions. The 10 nm thick minority carrier reflectors with doping concentrations of 10^{19} cm^{-3} are placed right below the top contact and above the bottom contact to reduce recombination loss. In the real devices, heavily doped n+ substrate ($2\text{--}3 \times 10^{18} \text{ cm}^{-3}$) serves as a bottom minority reflector, and the p-doping near the tip is increased to serve as a top minority reflector.

In Figure 2b, c, and d we show the J_{sc} , V_{oc} , and PCE as functions of n-type base doping concentration. For the axial junction, increasing the doping concentration reduces J_{sc} . Nanowires usually exhibit shorter minority diffusion length than bulk, so the built-in electric field in the junction depletion region contributes significantly to the total collection of carriers. With increasing doping in the n-type base of axial junction, both the junction depletion region width, which defines the carrier drift zone, and the mobility, which determines carrier diffusion, are reduced. The open circuit voltage however increases with increasing doping concentration due to the larger built-in potential. The overall efficiency does not change much with the increasing doping concentration. For the radial junction, the short circuit current is very high when the base doping is higher than 10^{17} cm^{-3} . However, it drops sharply when the doping is smaller than 10^{17} cm^{-3} . The open circuit voltage and the efficiency of the radial junction have similar trends. The precise measurement of spatial distribution of dopant in nanowires remains a great challenge in this field and has not been fully investigated since most techniques and physics used for bulk material could not be directly applied to nanoscale materials. However, people did observe doping⁵⁴ and material composition¹⁶ variation along a nanowire over 1 order of magnitude. Emerging technologies such as atom probe tomography⁵⁵ or single wire Hall effect measurement⁵⁶ could provide us with more powerful tools to obtain detailed doping information in a nanowire.

We can gain insight into the difference between the J – V characteristics of axial and radial junctions in the low doping region from Figure 2e and f. Figure 2e shows the band diagrams across the center of the wires (A–A' for the axial junction and B–B' for the radial junction) under the AM 1.5G solar spectrum and short circuit condition and the corresponding hole concentration mapping in the dark under thermal equilibrium conditions with a base doping of 10^{16} cm^{-3} . In the axial junction, the n-type region is fully depleted by surface states under thermal equilibrium, as one can tell from the fact that the hole concentration is close to the intrinsic carrier concentration of GaAs ($2.1 \times 10^6 \text{ cm}^{-3}$, 300 K). However, under illumination, the nanowire behaves as a normal p–i–n junction solar cell (see band diagram) because the surface states are largely filled by light-generated carriers. There is a gradual band bending along the axial direction near the junction at the

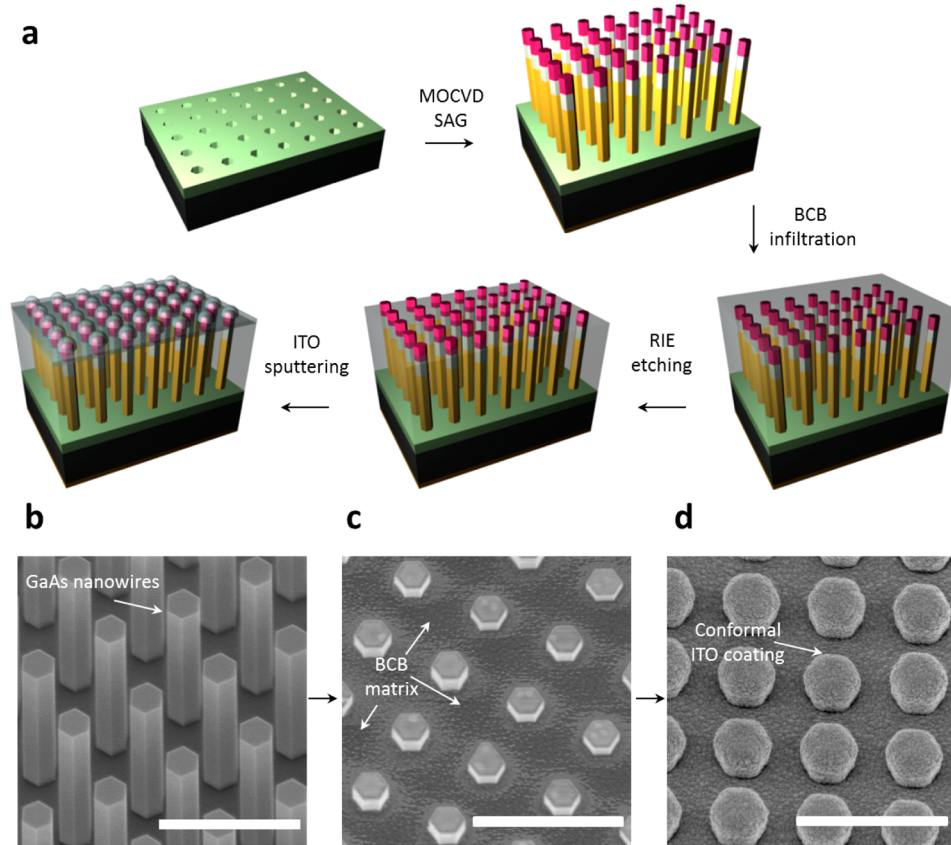


Figure 3. Solar cell fabrication process and SEM images. (a) Fabrication steps of GaAs nanowire array solar cells with axial junction: (i) electron beam lithography to form hole array in silicon nitride mask, (ii) SAG of p–i–n GaAs nanowire using MOCVD, (iii) BCB infiltration, (iv) RIE to expose nanowire tips, and (v) ITO deposition. (b) 30° tilted SEM image of as grown vertical GaAs nanowire array on GaAs (111)B substrate. (c) SEM image after nanowires are embedded in BCB and etched by RIE to expose short tips. (d) SEM image after coating of ITO film by sputtering. A conformal dome-like cap is formed on the tips of nanowires.

heights between 2 and 2.4 μm (intrinsic segment is between 2.35 and 2.4 μm). This causes an electric field pointing upward, which helps the extraction of the light-generated carriers near the tip of the nanowire. In a radial junction, when the core region of the nanowire is lightly doped, the p-type shell will cause an inversion of the core carrier type to also be p-type. The structure is hence equivalent to a p-type nanowire with a very thin n-type emitter at the bottom as can be seen in the band diagram along B–B' in Figure 2e. This can further be confirmed by checking the cross-sectional (C–C') band diagrams in Figure 2f, which shows the band is almost flat. The minority carriers thus need to diffuse through the entire length of nanowire to reach the bottom and get extracted, under which circumstance an extremely low J_{sc} is expected.

In principle the heavily doped radial junction device can outperform the axial junction due to its excellent carrier collection efficiency and its high tolerance to surface effects. However, high doping in the base is usually undesirable because it reduces mobility and diffusion length. State-of-the-art thin film GaAs solar cells normally use a base doping concentration of the order of magnitude of 10^{17} cm^{-3} . The possibility of using lower doping in the axial junction provides us with more optimization space and a more robust design. Moreover, as mentioned before, the axial junction is an indispensable intermediate step toward a multijunction nanowire solar cell device with three or more junctions. The systematic experimental study of the GaAs axial junction nanowire solar cell has not previously been performed.

To experimentally test the performance predicted by simulation, we fabricated and measured solar cells with 1 mm \times 1 mm area GaAs nanowire arrays. The schematic diagram of device structure has been shown in Figure 1a and the fabrication process is shown in Figure 3a (see Supporting Information for details). The n-type, intentionally undoped, and p-type segments are grown sequentially on a n+ (111)B substrate using SAG in MOCVD. The growth detail has been mentioned earlier in a separate paper.^{35,39} This growth method does not require metal catalyst as used in vapor–liquid–solid (VLS) method which is believed to incorporate along the growth and cause deep level traps.⁴⁶ The vapor-phase epitaxial nature of SAG can also avoid reservoir effects often encountered in VLS and achieve an abrupt junction interface. The background doping for the i-region is not known at this point but is believed to be much lower than the p and n region and may be in the range of 10^{14} – 10^{15} cm^{-3} based on literature.⁵³ A systematic study of the influence of varying the length of i-region is ongoing, and the result will be published elsewhere in the future. We believe that the i-region with an optimized length could help carrier collection to certain degree given the short diffusion length in nanowires. Nanowires are separated by 600 nm from center to center and are about 2.5 μm tall and 320 nm in diameter, unless otherwise stated, to achieve nearly optimized absorption of AM 1.5G solar irradiation. Although the nanowires only cover less than 20% of the total area, they could potentially absorb close to 90% of the incident sun light. It is been widely studied that resonant

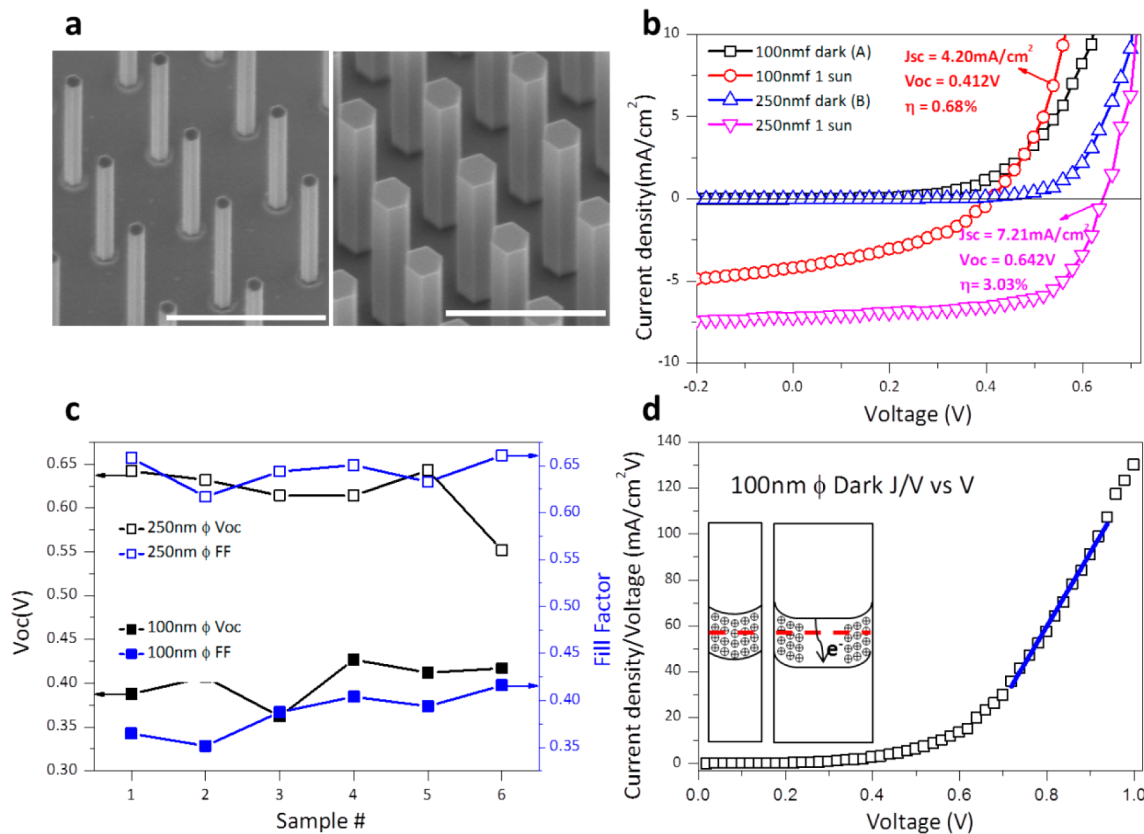


Figure 4. Comparison between performance of nanowires with 100 nm diameter and 250 nm diameter. (a) 30° tilted SEM images of nanowires with diameter of 100 nm (sample A) and 250 nm (sample B). (b) J – V curves of typical devices made from 100 and 250 nm thick nanowires in dark and under AM 1.5 solar spectrum. (c) V_{oc} (black) and FF (blue) of six devices from each batch. (d) J / V – V curve of the device with 100 nm nanowires shown in (b) which shows a linear region marked by the blue line. Insets are schematics of a fully depleted thin wire and of a partially depleted thick wire that still has a conductive channel in the center.

modes would allow light absorption in nanowires to significantly exceed the ray optics limit given just a fraction of the material consumed in a bulk device.^{11,21} Figure 3b is scanning electron microscopy (SEM) image taken at a 30° tilted angle. Nanowires distribute uniformly in the electron beam lithography (EBL) defined template and exhibit 6-fold symmetric cross section consisting of sidewalls parallel to {110} family planes which indicate high crystal quality.

After growth, nanowire arrays are planarized and etched to only expose the tip of p-type emitter. Eventually ITO is deposited as a transparent front contact (Figure 3a), while AuGe is alloyed to the backside of the substrate to form ohmic contact. The sheet resistances of planar ITO film is about 10 Ohm/ \square measured by four-probe method. The highly conductive ITO film allows us to achieve low series resistance without forming additional metal fingers on top of ITO as will be shown later. Sputtering provides a conformal layer of ITO on the nonplanar top surface and forms a dome shape cladding over the nanowire tip which helps to concentrate the incident light near the junction region as has been seen in Figure 1e and also pointed out by Mariani et al.¹⁵ Figure 3c shows the 30° tilted SEM image of nanowire array after BCB infiltration and reactive ion etching (RIE). About 100 nm tip is exposed for contacting. Figure 3d shows ITO film conformally wrapping the nanowire tips to ensure good conductivity at the front electrode. Basically the high uniformity is inherited from EBL-made pattern by the subsequent process and demonstrates the

superior capability of SAG in controlling the morphology and location of nanowires.

Because of the high density of surface states, carrier transport in GaAs nanowires is known to be significantly affected by the surface-to-volume ratio. For nanowires with surface Fermi level pinned at midgap, Chang et al.⁴⁷ pointed out the majority carriers would be nearly depleted if wire diameter is less than 100 nm, resulting in a less conductive channel which is also observed in our simulation. Furthermore, a considerable portion of minority carriers would be captured by surface states and subsequently annihilate through recombination for a thin wire. Thus, one expects significant loss of J_{sc} when the nanowire diameter gets extremely small. Figure 4a shows SEM images of the 30° tilted nanowire arrays used for two sets of devices. Both samples are around 1.5 μm tall with a 300 nm deep junction. Sample A consists of nanowires about 100 nm in diameter, while the wires in sample B are close to 250 nm in diameter. J – V characteristics are measured under dark conditions as well as under AM 1.5G solar spectrum at 1 sun illumination intensity (100 mW/cm²) using a solar simulator (Photo Emission Tech). Distinct J – V curves can be seen in Figure 4b for representative devices made from these two batches. Remarkably improved performance is obtained for nanowires of 250 nm than nanowires of a 100 nm diameter due to both larger J_{sc} and higher V_{oc} . Another important parameter reflecting how closely a device resembles an ideal diode is fill factor (FF) defined by the ratio of maximum power output to the product of I_{sc} and V_{oc} . Figure 4c shows the V_{oc} and FF of all

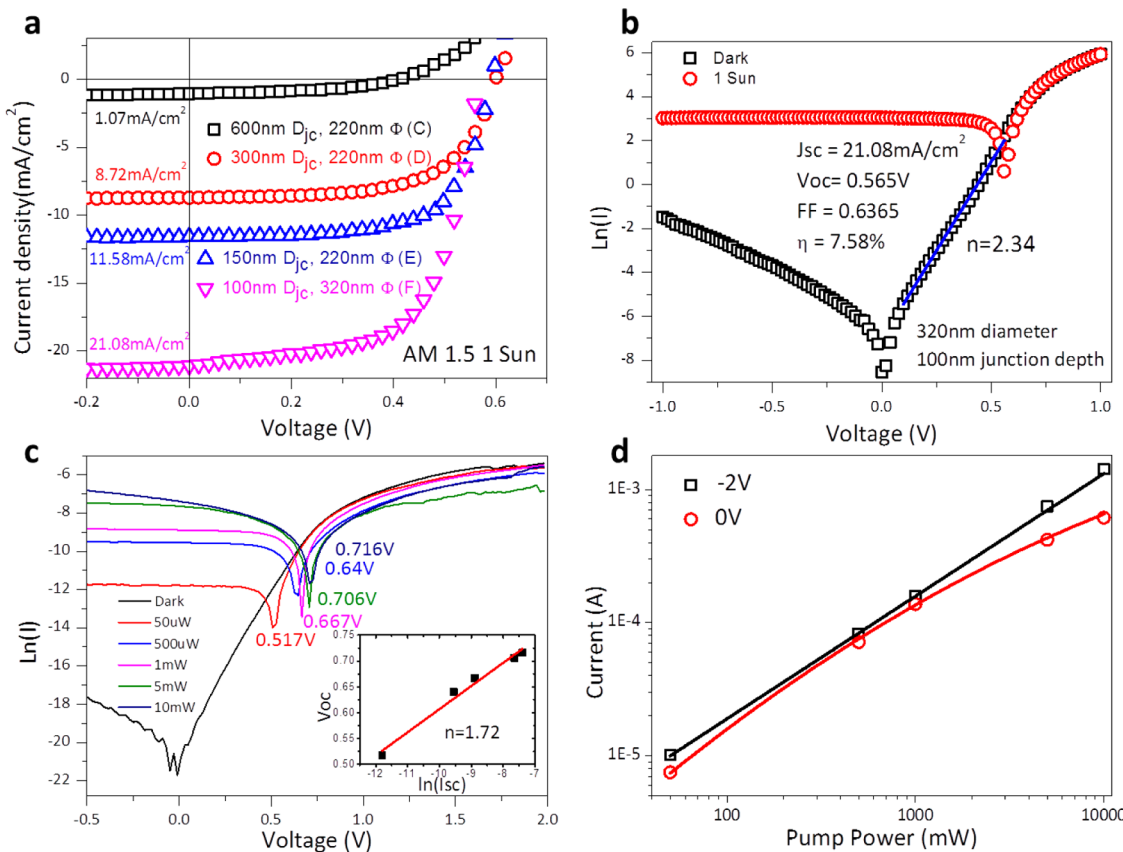


Figure 5. Junction depth dependency and J – V under varied light intensity. (a) J – V curves of devices with different junction depths between 100 and 600 nm under AM 1.5 solar spectrum. For the device with 100 nm junction depth, the diameter is increased to 320 nm. (b) Dark and AM 1.5 J – V curves of the device with 100 nm junction depth and 320 nm diameter shown in (a) plotted in semilogarithmic scale. The ideality factor is found to be 2.34. (c) J – V curves of the device with 150 nm junction depth and 220 nm diameter shown in (a) under different illuminating powers between 50 μW and 10 mW from an 850 nm laser. V_{oc} of 0.716 V is observed under the highest light intensity. Insets shows the curve of V_{oc} vs $\ln(I_{\text{sc}})$ with the extracted ideality factor to be 1.72. (d) Current versus pump power for the device shown in (c) at -2 and 0 V bias.

the samples from batch A and B, and each batch contains six individual devices. From this figure, the FF of sample B is much higher than sample A on average following the same trend as V_{oc} . In larger diameter nanowires, fewer carriers will recombine at the surface leading to higher J_{sc} . On the other hand if the entire n-type base is depleted as a result of a small diameter, then the built-in potential across the p-i-n junction will definitely be smaller than an ideal junction because the Fermi-level in the n-type region is deeper into the bandgap than it would be in an ideal case. Moreover, plots of current density divided by voltage (J/V) versus V for sample A shows, after the diode turns on, J/V is proportional to V indicating strong quadratic dependence on voltage for dark current as shown in Figure 4d. This phenomenon can be attributed to space charge limited (SCL) transport in a fully depleted crystal which was recently modeled and discussed for gallium nitride nanowires⁴⁸ and indium arsenide nanowires.⁴⁹

In addition to nanowire diameter we studied another important design parameter which is the length of the p-emitter region, also mentioned as junction depth (D_{jc}) interchangeably in this paper. As has been shown in Figure 1e, upon illumination of the solar spectrum, the carrier generation hot spot is located very close to the nanowire tip due to the high absorption coefficient of GaAs over most of the solar spectrum as well as the concentrating effect from the ITO cap. On the other hand, to achieve low resistance ohmic contact between ITO and GaAs, the p-doping near the top is

usually sufficiently high leading to relatively shorter minority carrier lifetime. Thus, we want to minimize carrier loss in the p-region while keeping a good contact to ITO. Experimentally we varied the length of p-segment between 600 and 100 nm by adjusting the growth time. As shown in Figure 5a a steady increase in short circuit current can be observed when we decrease the junction depth. Typical devices show J_{sc} of 1.07, 8.52, and 11.58 mA/cm^2 for devices with a 220 nm diameter and nominally 600 nm (sample C), 300 nm (sample D), and 150 nm (sample E) deep junctions, respectively. Shallower junctions also feature higher V_{oc} in general. The batch with 600 nm deep junction (sample C) exhibits relatively low V_{oc} around 350 mV, and in contrast, devices in the batch with a 150 nm deep junction (sample E) have a V_{oc} approaching 650 mV. In batch F we further reduce junction depth to 100 nm and also increase the diameter to around 320 nm. We observe a tremendous increase of J_{sc} to above 20 mA/cm^2 with the highest being 23.28 mA/cm^2 . Although both nanowire diameter and junction depth affect the solar cell performance, we believe the nanowire diameter is the more dominant factor, especially for nanowires with a junction depth less than 300 nm. More discussion can be found in the Supporting Information. Figure 5b shows the dark and 1 Sun J – V curve of the best device from batch F plotted as a semilogarithmic plot. The dark characteristic shows a good rectifying behavior with an on-off ratio of 1.89×10^5 at $\pm 1 \text{ V}$. The dark current at -1 V is only about 100 nA for a 1 mm^2 area also indicating a good junction.

The small leakage current could be attributed to the small total junction area possessed by axial junction geometry. The vapor phase growth of the junction should, in principle, produce a sharp junction with low leakage current. The ideality factor extracted from the intermediate forward bias regime is around 2.34. We believe that the greater-than-unity ideality factor is due to the existence of recombination current through surface states and space charge region in the undoped part. Further optimization of the length of the undoped segment is ongoing. This particular device shows J_{sc} of 21.08 mA/cm² and V_{oc} of 0.565 V. With a fill factor of 0.6365 the overall PCE is 7.58%. In a previous publication,³⁷ we have simulated and experimentally studied the role of substrate on photon absorption. Even though the substrate may absorb a small portion of the photons, because carrier generation is relatively far away from the p-i-n junction, the contribution of substrate to J_{sc} would be negligible. We thus expect the power conversion capability mainly comes from the nanowire array. The slightly lower V_{oc} here in sample F compared to sample D and E is due to the logarithmic dependence of V_{oc} on I_{sc} for an ideal diode which will be shown later; thus the increase of V_{oc} with a shallower junction depth is not as pronounced as J_{sc} and sometimes can be masked by the device-to-device variation as manifested by the red, blue, and pink curves in Figure 5a. We note that, in the device showing efficiency of 7.58%, the ITO may be in contact with the i-region for some of the nanowires as both the junction depth and the exposed nanowire tip length after BCB etching are about 100 nm. By further optimizing the process and control of exposed tip length we may be able to achieve even better performance. All of the devices discussed so far are summarized in Table 1.

Table 1. Characteristics of Devices with Different Diameters and Junction Depths

device	diameter (nm)	junction depth (nm)	J_{sc} (mA/cm ²)	V_{oc} (V)	efficiency (%)
A	100	300	4.20	0.412	0.68
B	250	300	7.21	0.642	3.03
C	220	600	1.07	0.410	0.21
D	220	300	8.72	0.600	3.30
E	220	150	11.58	0.592	4.62
F	320	100	21.08	0.565	7.58
G (see SI)	320	300	21.21	0.511	6.56

When a nonideal p-n junction with a series resistance is considered with respect to the forward bias voltages, the current across a p-n diode is given by

$$I = I_0 \left[\exp\left(\frac{q(V - IR_s)}{nkT}\right) - 1 \right]$$

To accurately determine the series resistance, we can differentiate both side of the current equation and obtain (Cheung's method⁵⁰):

$$\frac{dV}{d(\ln I)} = \frac{nkT}{q} + IR_s$$

A plot of $dV/d(\ln I)$ versus I will be linear and gives R_s as the slope and nkT/q as the y-axis intercept. The extracted values of ideality factor and series resistance are 2.2 and 41 Ω (see Supporting Information, Figure S2), respectively.

Finally, we measured device response under varied illumination power. Figure 5c shows the J - V curves of device with 300 nm junction depth and 220 nm diameter (red curve in Figure 4b) in dark and at various illumination powers from an 850 nm laser plotted in semilogarithmic coordinates. The short circuit current increases steadily when power is increased from 50 μW to 5 mW and starts to saturate at higher powers which indicates reduced quantum efficiency. This behavior is due to increased voltage drop across series resistance under high illumination as well as carrier screening effect which reduces the internal electrical field when the carrier concentration is sufficiently high. Similar trend was observed in photodetector devices made from similar nanowires recently in our group.⁵¹ By applying a larger reverse bias, we can rebuild the strength of electrical field so we can see incremental change of current scales with illumination power at -2 V applied bias (Figure 5d), while the current at short circuit fails to track under high illumination intensity. The open circuit voltage increases steadily with increasing pump power. V_{oc} for the highest illumination reaches 0.72 V. Neglecting the small series resistance the diode I - V behavior under illumination could be described as

$$\begin{aligned} I &= I_0 \left(\exp\left(\frac{qV}{nkT}\right) - 1 \right) - I_L \\ &\approx I_0 \left(\exp\left(\frac{qV}{nkT}\right) - 1 \right) - I_{sc} \end{aligned}$$

So we can extract V_{oc} as a function of short circuit current:

$$V_{oc} = V(I = 0) = \frac{nkT}{q} \ln\left(\frac{I_{sc}}{I_0} + 1\right)$$

The inset of Figure 5c is the plot of V_{oc} versus $\ln(I_{sc})$, and the slope is nkT/q , from which we extracted the ideality factor to be 1.72.

From the results shown in Figure 5a, it is apparent that a shallow junction is essential for unpassivated GaAs nanowire solar cells to capture minority carriers generated close to the tip which would otherwise recombine quickly in the heavily doped p-emitter region. To better understand the underlying physical mechanism, we simulated the carrier generation profile under monochromatic light of different wavelengths and measured the spectrum response of the four devices shown in Figure 5a. The integration of product of EQE and AM 1.5 photon density resulted in J_{sc} similar to the value measured experimentally in Figure 5a. From Figure 6a we can see most of the shorter wavelength light (400 nm) is absorbed near the wire surface, while a bigger portion of longer wavelength light (800 nm) is absorbed deeper into the bulk of the nanowire. Carriers generated by shorter wavelengths thus are more likely to recombine at the surface and annihilate. That explains why the EQE of the shorter wavelength is always lower than the EQE of longer length for all four devices shown in Figure 6b. The surface-to-volume ratio decreases with increasing diameter so a smaller portion of the total generated carriers are distributed in the vicinity of surface for thicker nanowires which leads to higher EQE in 320 nm thick nanowire than in 220 nm thick nanowire with similar junction depth over a broad range of wavelength. To interpret the junction depth dependency of J_{sc} we conduct cathodoluminescence (CL) measurement (Horiba) built in the Hitachi S-4800 SEM. To excite luminescence from a single nanowire, the sample was cleaved so that electron beam

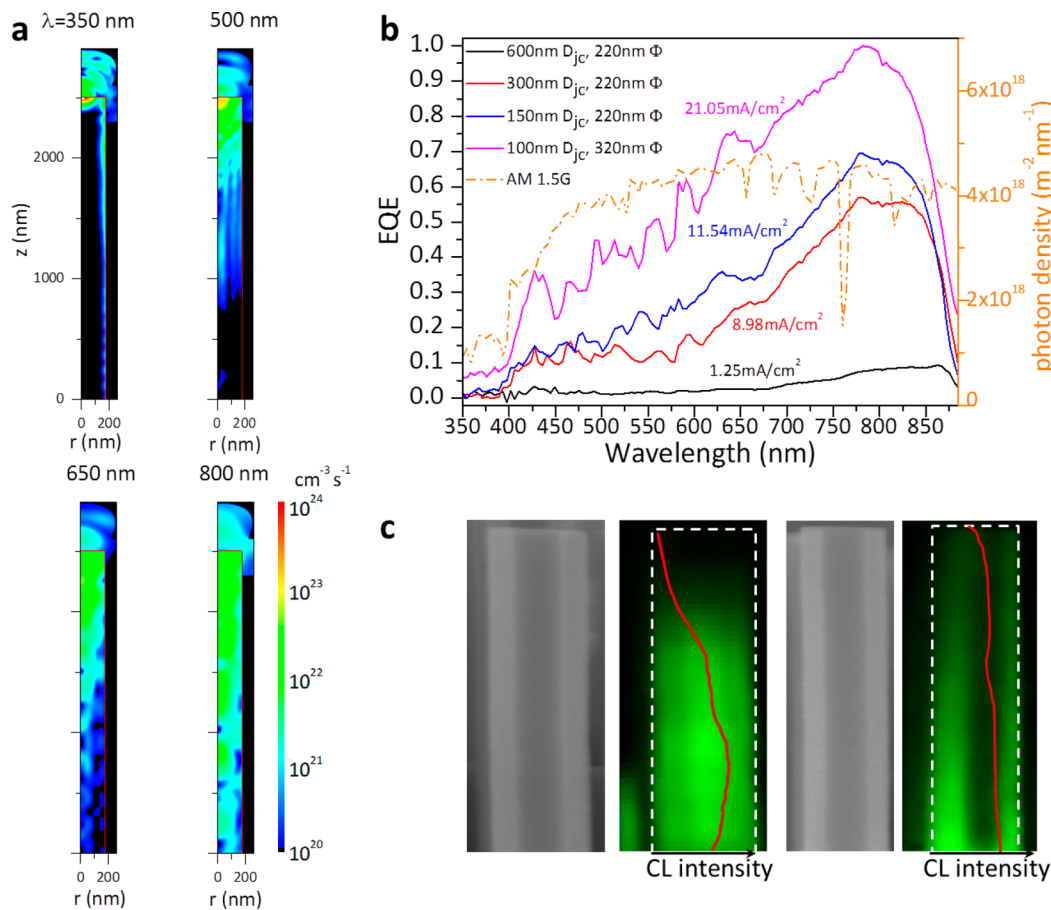


Figure 6. Spectrum response and Cathodoluminescence mapping. (a) Carrier generation rate profile under monochromatic light of different wavelengths between 350 and 800 nm. All of the light intensities are 100 mW/cm². Nanowires are 2.5 μ m tall and 350 nm in diameter with a 600 nm pitch. Nanowires are surrounded by BCB and covered by ITO on top. (b) External quantum efficiency (left y-axis) vs wavelength of the four devices shown in Figure 5a. The dash-dot curve is the photon intensity of AM 1.5G solar spectrum (right y-axis). J_{sc} of each device are calculated by integrating the product of EQE and photon intensity over the range of 350–880 nm and are indicated in the plot. (c) SEM images and normalized cathodoluminescence mapping at wavelength of 865 nm for nanowires with 400 nm deep junction (left) and 100 nm deep junction (right). Red curves are relative CL intensity along the center of each nanowire.

can be focused and scanned normal to the sidewall surface. The acceleration voltage was kept at 5 kV to ensure that no electrons penetrate the wire to be examined and cause luminescence from other wires behind. SEM micrographs and normalized CL intensity maps at 865 nm from two single nanowires, one with 400 nm long p-region (left) and the other 100 nm long p-region (right), are plotted in Figure 6c, and the line scans from the center of the two wires are also superimposed. The top 300 nm of the wire with a 400 nm deep junction does not emit efficiently. The intensity gradually increases with distance from the top of the nanowire and eventually saturates when the electron beam moves toward the bottom of the wire. This trend qualitatively agrees with the aforementioned model that nonradiative recombination processes are dominant in the p-doped region due to the high impurity concentration introduced to achieve good ohmic contact. On the other hand the luminescent intensity is much more uniform for the wire with only 100 nm long p-region. The luminescence intensity gradient along the wire is due to the fact that electron beam with 5 kV acceleration has 200–300 nm interaction volume upon impinging at the surface although the junction itself is considered more abrupt given the vapor phase epitaxy employed. In addition, those holes generated close to the junction have a higher probability of being swept by the

junction before they radiatively recombine, while those holes generated far from the junction are more likely to recombine in the n-layer. The short radiative recombination lifetime and high nonradiative recombination rate observed in the p-emitter may well explain the increasing EQE with decreasing junction depth seen in Figure 6b, as less carriers would be lost in the p-emitter when its length is reduced.

Last but not least, the V_{oc} measured from our devices is still considerably lower than the values reported for GaAs planar p–n junctions, which can be attributed to several factors. In nanowire solar cells because all of the nanowires are isolated from each other, we need to form a front contact that can access all of them. This has been shown to be detrimental to V_{oc} in planar solar cells where one tries to passivate most of the emitter surface and to only make contact on area as small as possible.⁵² Intrinsic surface states together with surface defects introduced by processes such as etching and sputtering can lead to significant recombination at the nanowire/ITO interface, leading to lower V_{oc} . The presence of band bending and doping variation in the radial direction will cause an inhomogeneous barrier at the junction. Since the lower barrier part dominates the current conduction, V_{oc} is also largely determined by the lowest barrier height across the intersection. In principle, a window layer with a larger band gap and low surface states

density could passivate the GaAs nanowire surface. This part of work is still ongoing, and we are studying the passivation effect of shells consist of AlGaAs, GaAsP, and InGaP. One issue that needs to be paid extra care is that the presence of passivation layer should not introduce a significant shunting path between p- and n-regions which requires low unintentional doping in the shell and low interface trap density. Furthermore, a rigorous assessment of the doping concentration within the nanowire is necessary to determine the build-in potential which sets the upper limit of V_{oc} .

In summary, we carried out optical simulation to predict the optimized wire array geometry for maximum light absorption. We then compared the advantages and limitations of both axial junction and radial junction design. We experimentally demonstrated solar cells realized by arrays of GaAs nanowires with axial p-i-n junction which are grown by versatile selective area growth method using mass production compatible MOCVD technique. A nanowire array with a low filling ratio turns out to be highly absorptive. Systematic studies on the effect of the diameter reveal that thicker nanowires are favorable because of the high surface recombination velocity on the bare GaAs nanowire surface. Junction depth also plays a significant role in carrier collection efficiency. By reducing junction depth to around 100 nm and keeping diameter at 320 nm, we are able to achieve efficiencies as high as 7.58%. Under concentrated 850 nm light, a V_{oc} as high as 0.716 V has been obtained. The results demonstrate that GaAs nanowires are good candidates for high-efficiency and low-cost solar energy conversion and open up great opportunities for the next generation photovoltaics based on multijunction devices composed of lattice mismatched material systems.

■ ASSOCIATED CONTENT

Supporting Information

Details on simulation, nanowire growth, solar cell fabrication, and extraction of series resistance based on Cheung's method. This material is available free of charge via the Internet at <http://pubs.acs.org>.

■ AUTHOR INFORMATION

Corresponding Authors

*E-mail: dapkus@usc.edu (P.D.D.).

*E-mail: chongwuz@usc.edu (C.Z.).

Notes

The authors declare no competing financial interest.

■ ACKNOWLEDGMENTS

This material is based upon work supported as part of the Center for Energy Nanoscience (CEN), an Energy Frontier Research Center (EFRC) funded by the U.S. Department of Energy, Office of Science and Office of Basic Energy Sciences under Award Number DE-SC0001013. Computing resources were provided by the USC Center for High Performance Computing and Communications. M. Y. was funded by USC Provost's Ph.D. Fellowship.

■ REFERENCES

- (1) Tian, B.; Zheng, X.; Kempa, T. J.; Fang, Y.; Yu, N.; Yu, G.; Huang, J.; Lieber, C. M. *Nature* **2007**, *449*, 885–889.
- (2) Garnett, E. C.; Yang, P. J. *J. Am. Chem. Soc.* **2008**, *130*, 9224–9225.
- (3) Tang, J.; Huo, Z.; Brittman, S.; Gao, H.; Yang, P. *Nat. Nanotechnol.* **2011**, *6*, 568–572.
- (4) Kempa, T. J.; Cahoon, J. F.; Kim, S.-K.; Day, R. W.; Bell, D. C.; Park, H.-G.; Lieber, C. M. *Proc. Natl. Acad. Sci. U.S.A.* **2012**, *109*, 1407–1412.
- (5) Czaban, J. A.; Thompson, D. A.; LaPierre, R. R. *Nano Lett.* **2008**, *9*, 148–154.
- (6) Goto, H.; Nosaki, K.; Tomioka, K.; Hara, S.; Hiruma, K.; Motohisa, J.; Fukui, T. *Appl. Phys. Express* **2009**, *2*, 035004.
- (7) Mariani, G.; Wong, P.-S.; Katzenmeyer, A. M.; Léonard, F.; Shapiro, J.; Huffaker, D. L. *Nano Lett.* **2011**, *11*, 2490–2494.
- (8) Wei, W.; Bao, X.-Y.; Soci, C.; Ding, Y.; Wang, Z.-L.; Wang, D. *Nano Lett.* **2009**, *9*, 2926–2934.
- (9) Shin, J. C.; Kim, K. H.; Yu, K. J.; Hu, H.; Yin, L.; Ning, C.-Z.; Rogers, J. A.; Zuo, J.-M.; Li, X. *Nano Lett.* **2011**, *11*, 4831–4838.
- (10) Tomioka, K.; Tanaka, T.; Hara, S.; Hiruma, K.; Fukui, T. *IEEE J. Sel. Top. Quantum Electron.* **2011**, *17*, 1112–1129.
- (11) Hu, S.; Chi, C.-Y.; Fountain, K. T.; Yao, M.; Atwater, H. A.; Dapkus, P. D.; Lewis, N. S.; Zhou, C. *Energy Environ. Sci.* **2013**, *6*, 1879–1890.
- (12) Zhu, J.; Hsu, C.-M.; Yu, Z.; Fan, S.; Cui, Y. *Nano Lett.* **2009**, *10*, 1979–1984.
- (13) Putnam, M. C.; Boettcher, S. W.; Kelzenberg, M. D.; Turner-Evans, D. B.; Spurgeon, J. M.; Warren, E. L.; Briggs, R. M.; Lewis, N. S.; Atwater, H. A. *Energy Environ. Sci.* **2010**, *3*, 1037–1041.
- (14) Mariani, G.; Scofield, A. C.; Hung, C.-H.; Huffaker, D. L. *Nat. Commun.* **2013**, *4*, 1497.
- (15) Mariani, G.; Zhou, Z.; Scofield, A.; Huffaker, D. L. *Nano Lett.* **2013**, *13*, 1632–1637.
- (16) Holm, J. V.; Jørgensen, H. I.; Krogstrup, P.; Nygård, J.; Liu, H.; Aagesen, M. *Nat. Commun.* **2013**, *4*, 1498.
- (17) Krogstrup, P.; Jørgensen, H. I.; Heiss, M.; Demichel, O.; Holm, J. V.; Aagesen, M.; Nygård, J.; Fontcuberta i Morral, A. *Nat. Photonics* **2013**, *7*, 306–310.
- (18) Cui, Y.; Wang, J.; Plissard, S. R.; Cavalli, A.; Vu, T. T. T.; van Veldhoven, R. P. J.; Gao, L.; Trainor, M.; Verheijen, M. A.; Haverkort, J. E. M.; Bakkers, E. P. A. M. *Nano Lett.* **2013**, *13*, 4113–4117.
- (19) Nakai, E.; Yoshimura, M.; Tomioka, K.; Fukui, T. *Jpn. J. Appl. Phys.* **2013**, *52*, 055002.
- (20) Gutsche, C.; Lysov, A.; Braam, D.; Regolin, I.; Keller, G.; Li, Z.-A.; Geller, M.; Spasova, M.; Prost, W.; Tegude, F.-J. *Adv. Funct. Mater.* **2012**, *22*, 929–936.
- (21) Wallentin, J.; Anttu, N.; Asoli, D.; Huffman, M.; Åberg, I.; Magnusson, M. H.; Siefer, G.; Fuss-Kailuweit, P.; Dimroth, F.; Witzigmann, B.; Xu, H. Q.; Samuelson, L.; Deppert, K.; Borgström, M. T. *Science* **2013**, *339*, 1057–1060.
- (22) King, R. R.; Law, D. C.; Edmondson, K. M.; Fetzer, C. M.; Kinsey, G. S.; Yoon, H.; Sherif, R. A.; Karam, N. H. *Appl. Phys. Lett.* **2007**, *90*, 183516.
- (23) Geisz, J. F.; Kurtz, S.; Wanlass, M. W.; Ward, J. S.; Duda, A.; Friedman, D. J.; Olson, J. M.; McMahon, W. E.; Moriarty, T. E.; Kiehl, J. T. *Appl. Phys. Lett.* **2007**, *91*, 023502.
- (24) Geisz, J. F.; Friedman, D. J.; Ward, J. S.; Duda, A.; Olavarria, W. J.; Moriarty, T. E.; Kiehl, J. T.; Romero, M. J.; Norman, A. G.; Jones, K. M. *Appl. Phys. Lett.* **2008**, *93*, 123505.
- (25) Guter, W.; Schone, J.; Philipps, S. P.; Steiner, M.; Siefer, G.; Wekkeli, A.; Welser, E.; Oliva, E.; Bett, A. W.; Dimroth, F. *Appl. Phys. Lett.* **2009**, *94*, 223504.
- (26) Derkacs, D.; Jones-Albertus, R.; Suarez, F.; Fidaner, O. *J. Photon. Energy* **2012**, *2*, 021805–8.
- (27) Gudiksen, M. S.; Lauhon, L. J.; Wang, J.; Smith, D. C.; Lieber, C. M. *Nature* **2002**, *415*, 617–620.
- (28) Glas, F. *Phys. Rev. B* **2006**, *74*, 121302.
- (29) Sburlan, S.; Dapkus, P. D.; Nakano, A. *Appl. Phys. Lett.* **2012**, *100*, 163108.
- (30) Chuang, L. C.; Moewe, M.; Chase, C.; Kobayashi, N. P.; Chang-Hasnain, C.; Crankshaw, S. *Appl. Phys. Lett.* **2007**, *90*, 043115.
- (31) Ertekin, E.; Greaney, P. A.; Chrzan, D. C.; Sands, T. D. *J. Appl. Phys.* **2005**, *97*, 114325.
- (32) Tomioka, K.; Kobayashi, Y.; Motohisa, J.; Hara, S.; Fukui, T. *Nanotechnology* **2009**, *20*, 145302.

- (33) Mårtensson, T.; Svensson, C. P. T.; Wacaser, B. A.; Larsson, M. W.; Seifert, W.; Deppert, K.; Gustafsson, A.; Wallenberg, L. R.; Samuelson, L. *Nano Lett.* **2004**, *4*, 1987–1990.
- (34) Moewe, M.; Chuang, L. C.; Crankshaw, S.; Chase, C.; Chang-Hasnain, C. *Appl. Phys. Lett.* **2008**, *93*, 023116.
- (35) Yao, M.; Madaria, A. R.; Chi, C.; Huang, N.; Lin, C.; Povinelli, M. L.; Dapkus, P. D.; Zhou, C. *SPIE Defense, Security, Sensing* **2012**, 837314.
- (36) Ningfeng, H.; Chenxi, L.; Michelle, L. P. *J. Opt.* **2012**, *14*, 024004.
- (37) Huang, N.; Lin, C.; Povinelli, M. L. *J. Appl. Phys.* **2012**, *112*, 064321.
- (38) Wen, L.; Zhao, Z.; Li, X.; Shen, Y.; Guo, H.; Wang, Y. *Appl. Phys. Lett.* **2011**, *99*, 143116.
- (39) Madaria, A. R.; Yao, M.; Chi, C.; Huang, N.; Lin, C.; Li, R.; Povinelli, M. L.; Dapkus, P. D.; Zhou, C. *Nano Lett.* **2012**, *12*, 2839–2845.
- (40) Lin, C.; Povinelli, M. L. *Opt. Express* **2009**, *17*, 19371–19381.
- (41) Lin, C.; Povinelli, M. L. *Opt. Express* **2011**, *19*, A1148–A1154.
- (42) Lin, C.; Huang, N.; Povinelli, M. L. *Opt. Express* **2012**, *20*, A125–A132.
- (43) Kelzenberg, M. D.; Boettcher, S. W.; Petykiewicz, J. A.; Turner-Evans, D. B.; Putnam, M. C.; Warren, E. L.; Spurgeon, J. M.; Briggs, R. M.; Lewis, N. S.; Atwater, H. A. *Nat. Mater.* **2010**, *9*, 239–244.
- (44) Heurlin, M.; Wickert, P.; Fält, S.; Borgström, M. T.; Deppert, K.; Samuelson, L.; Magnusson, M. H. *Nano Lett.* **2011**, *11*, 2028–2031.
- (45) Colombo, C.; Heiß, M.; Grätzel, M.; Fontcuberta i Morral, A. *Appl. Phys. Lett.* **2009**, *94*, 173108.
- (46) Breuer, S.; Pfüller, C.; Flissikowski, T.; Brandt, O.; Grahn, H. T.; Geelhaar, L.; Riechert, H. *Nano Lett.* **2011**, *11*, 1276–1279.
- (47) Chang, C.-C.; Chi, C.-Y.; Yao, M.; Huang, N.; Chen, C.-C.; Theiss, J.; Bushmaker, A. W.; LaLumondiere, S.; Yeh, T.-W.; Povinelli, M. L.; Zhou, C.; Dapkus, P. D.; Cronin, S. B. *Nano Lett.* **2012**, *12*, 4484–4489.
- (48) Talin, A. A.; Léonard, F.; Swartzentruber, B. S.; Wang, X.; Hersee, S. D. *Phys. Rev. Lett.* **2008**, *101*, 076802.
- (49) Katzenmeyer, A. M.; Léonard, F.; Talin, A. A.; Toimil-Molares, M. E.; Cederberg, J. G.; Huang, J. Y.; Lensch-Falk, J. L. *IEEE Trans. Nanotechnol.* **2011**, *10*, 92–95.
- (50) Cheung, S. K.; Cheung, N. W. *Appl. Phys. Lett.* **1986**, *49*, 85–87.
- (51) Seyed, M. A.; Yao, M.; O'Brien, J.; Wang, S. Y.; Dapkus, P. D. *Appl. Phys. Lett.* **2013**, *103*, 251109.
- (52) Zhao, J.; Wang, A.; Altermatt, P. P.; Wenham, S. R.; Green, M. A. *Sol. Energy Mater. Sol. Cells* **1996**, *41*–42, 87–99.
- (53) Kushibe, M.; Eguchi, K.; Funamizu, M.; Ohba, Y. *Appl. Phys. Lett.* **1990**, *56*, 1248–1250.
- (54) Dufouleur, J.; Colombo, C.; Garma, T.; Ketterer, B.; Uccelli, E.; Nicotra, M.; Fontcuberta i Morral, A. *Nano Lett.* **2010**, *10*, 1734–1740.
- (55) Allen, J. E.; Hemesath, E. R.; Pereira, D. E.; Lensch-Falk, J. L.; LiZ, Y.; Yin, F.; Gass, M. H.; Wang, P.; Bleloch, A. L.; Palmer, R. E.; Lauhon, L. J. *Nat. Nanotechnol.* **2008**, *3*, 168–173.
- (56) Storm, K.; Halvardsson, F.; Heurlin, M.; Lindgren, D.; Gustafsson, A.; Wu, P. M.; Monemar, B.; Samuelson, L. *Nat. Nanotechnol.* **2012**, *7*, 718–722.